LiNi$_{0.5}$Mn$_{1.5}$O$_4$ Thin Films Grown by Magnetron Sputtering under Inert Gas Flow Mixtures as High-Voltage Cathode Materials for Lithium-Ion Batteries

Hamideh Darjazi,[a] Iñaki Madinabeitia,[b, c, d] Maider Zarrabeitia,[b, g, h] Elena Gonzalo,[b] Begoña Acebedo,[b] S. Javad Rezvani,[e] Francisco José Fernández-Carretero,[d] Francesco Nobili,[a, f] Alberto García-Luis,[d] and Miguel Ángel Muñoz-Márquez*[a, b]

Delivering a commercial high-voltage spinel LiNi$_{0.5}$Mn$_{1.5}$O$_4$ (LNMO) cathode electrode for Li-ion batteries would result in a significant step forward in terms of energy density. However, the structural ordering of the spinel and particle size have considerable effects on the cathode material's cyclability and rate capability, which are crucial challenges to address. Here, a novel mid-frequency alternating current dual magnetron sputtering method was presented, using different Ar-N$_2$ gas mixtures ratios for the process gas to prepare various LNMO thin films with highly controlled morphology and particle size; as determined from X-ray diffraction, Raman spectroscopy and electron microscopy. It resulted in enhanced cycling and rate performance. This processing method delivered N-containing LNMO thin film electrodes with up to 15% increased discharge capacity at 1 C (120 mAh g^{-1}) with respect to standard LNMO (grown under only Ar gas flow) thin film electrodes, along with outstanding rate performance up to 10 C (99 mAh g^{-1}) in the operating voltage window 3.5–4.85 V *vs.* Li$^+$/Li. Besides, electrochemical impedance spectroscopy results showed that the intricate phase transitions present in standard LNMO electrodes were almost suppressed in N-containing LNMO thin films grown under different Ar-N$_2$ gas flow mixtures.

Introduction

In an attempt to strengthen the position of Li-ion batteries (LIBs) in the continuous quest for more efficient and better performant electric energy storage systems, the implementation of cathode materials is driven by their impact in terms of cost, safety, sustainability and electrochemical performance, especially high voltage and high power.[1]

Spinel lithium manganese oxide (LiMn$_2$O$_4$), also known as LMO, is one of the few cathode materials used in commercial LIBs.[2–4] The interest in this manganese oxide-based electrode material is nested in its low-cost, earth-abundance, environ-

mental friendliness, ease of preparation, and thermal stability, which is ultimately linked with improved safety. Beyond the economic and environmental perspective, the spinel LMO structure, with space group *Fd3m*, exhibits a closed-packed array of oxygen (32*e* sites), where Li and Mn atoms are located at 8*a* tetrahedral and 16*d* octahedral sites, respectively. Thus, intrinsically providing three-dimensional (3D) Li$^+$ ions pathways which facilitate Li$^+$ ions diffusion during cycling (Figure S1a).[5] However, the drawbacks of 3D tunnel structured spinel LMO material, *i.e.* fast capacity decay upon cycling, poor performance at high temperature due to Jahn-Teller distortions, and the disproportionation reaction of Mn^{3+}(solid) to Mn^{2+}(solution)

[a] Dr. H. Darjazi, Dr. F. Nobili, Dr. M. Á. Muñoz-Márquez
School of Science and Technology - Chemistry Division
University of Camerino
Via Madonna delle Carceri, ChIP, 62032 Camerino, Italy
E-mail: miguel.munoz@unicam.it

[b] Dr. I. Madinabeitia, Dr. M. Zarrabeitia, Dr. E. Gonzalo, B. Acebedo, Dr. M. Á. Muñoz-Márquez
Centre for Cooperative Research on Alternative Energies (CIC energiGUNE)
Basque Research and Technology Alliance (BRTA)
Alava Technology Park, Albert Einstein 48, 01510 Vitoria-Gasteiz, Spain

[c] Dr. I. Madinabeitia
Departamento de Física de la Materia Condensada, Facultad de Ciencia y Tecnología
Universidad del País Vasco
UPV/EHU, P.O. Box 644, 48080 Bilbao, Spain

[d] Dr. I. Madinabeitia, Dr. F. J. Fernández-Carretero, Dr. A. García-Luis
TECNALIA, Basque Research and Technology Alliance (BRTA)
Parque Científico y Tecnológico de Gipuzkoa, Mikeletegi Pasealekua 2, 20009 Donostia-San Sebastián, Spain

[e] Dr. S. Javad Rezvani
School of Science and Technology - Physics Division
University of Camerino
Via Madonna delle Carceri 9B, 62032 Camerino, Italy

[f] Dr. F. Nobili
GISEL-Centro di Riferimento Nazionale per i Sistemi di Accumulo Elettrochimico di Energia, INSTM
via G. Giusti 9, 50121 Firenze, Italy

[g] Dr. M. Zarrabeitia
Present address
Helmholtz Institute Ulm (HIU)
Helmholtzstrasse 11, 89081, Ulm, Germany

[h] Dr. M. Zarrabeitia
Present address
Karlsruhe Institute of Technology (KIT)
P.O. Box 3640, 76021, Karlsruhe, Germany

and Mn^{4+} (solid), have been determined as main challenges that are currently limiting their practical application.[5–8]

To overcome these obstacles, one of the approaches is the partial replacement of Mn by Ni, resulting in the formation of spinel $LiNi_{0.5}Mn_{1.5}O_4$ (LNMO).[9] Indeed, LNMO has become one of the most studied positive electrodes for developing LIBs thanks to its enhanced cycling behavior, namely, the high operating voltage of 4.7 V vs. Li^+/Li and good specific capacity of 147 mAh g^{-1}.[10–12]

Two different LNMO crystallographic structures exist, linked to various Mn^{4+} and Ni^{2+} ions arrangements in the lattice.[13,14] One is the ordered LNMO, $P4_332$ space group (SG), where the Ni, Mn, Li, and O atoms occupy $4b$, $12d$, $8c$, and $8c/24e$ positions, respectively (Figure S1c). This structure displays a cation ordering so that the oxidation state of Mn is exclusively Mn^{4+}, which can isolate the active $Ni^{2+,3+,4+}$ redox centers, resulting in poor C-rate capability response.[9,13,15,16] The other possible structure is the disordered face-centered LNMO (space group $Fd3m$), where Mn has multi-valence states of Mn^{4+} and Mn^{3+}, and the atoms' arrangement is similar to LMO where Ni and Mn atoms are randomly located in $16d$ sites,[14,15] as shown in (Figure S1b). The presence of Mn^{3+} in the disordered spinel LNMO tends to increase the electrical conductivity of the material, hence enhancing the C-rate capability. However, at the same time, the concentration of Mn^{3+} should be limited as it can result in poor cycling stability due to Jahn-Teller distortion and associated side reactions.[9,16]

The morphology, particle size and cation ordering play a crucial role in addressing low cycling stability and C-rate capability, which are the main factors preventing the commercialization of LNMO.[9,17,18] This highlights the importance of the synthesis route and its control when aiming at the obtention of a competitive LNMO electrode. The electrochemical performance can be improved by using nanometric size materials,[19] such as nanoflakes,[20] nanofibers,[21,22] nanotubes,[23] and nanorods[24] due to their enhanced electronic transport and Li$^+$ ion shorter diffusion pathways, leading to faster insertion and extraction kinetics.[9,25] Many routes have been pursued to synthesize nanosized LNMO, namely, hydrothermal, solid-state, electrospinning, self-templating, co-precipitation, sputtering, etc.[9,18] In this framework, well-crystallized LNMO thin films with nanoflake morphology were prepared by mid-frequency alternating current (MF-AC) magnetron sputtering and post-annealing synthetic route that has been recently explored for the up-scaled production of LNMO as high-voltage Li-ion battery cathode.[26] Among all physical vapor deposition techniques, the MF-AC magnetron sputtering method has many advantages that make it a prominent candidate for industrial production of thin-film batteries, such as enabling the deposition of insulating thin films avoiding target poisoning (i), achieving a tighter control of the film chemical composition (ii), and working in the kHz range in contrast with the most extended radiofrequency (RF) magnetron sputtering (iii) which works in the MHz range, thus simplifying the power delivery and the power supply technology employed for the process while achieving higher deposition rates.

Herein, a nitridation process has been considered to improve the electronic conductivity of the LNMO and, ultimately, its electrochemical performance.[27–29] The MF-AC magnetron sputtering process in different Ar-N_2 gas mixture ratios has been proposed to prepare various LNMO thin films with highly controlled morphology, size, and crystallinity. This will help us to understand and control the role of LNMO nitridation in electrochemical performance.

Experimental Section

Thin films preparation

LNMO thin films were deposited using a semi-industrial *CemeCon CC800/8* unit based on the mid-frequency AC dual magnetron sputtering technology. The cathode deposition was performed onto 316 stainless-steel (SS) spacers of CR2032 coin cells that also acted as current collector (Hohsen Corp., thickness 0.5 mm, diameter 16 mm). Thus, simplifying the subsequent electrochemical investigations while preventing the utilization of more expensive Al or Cu current collectors. To hold the SS in front of the magnetron target and to ensure the homogeneous coating of a circular area (diameter of 12 mm) in the SS disc center, a circular mask with a centered 12 mm diameter was utilized. The distance between the SS substrate and target was set to 75 mm, and a maximum AC power of 300 W was applied to the single phase 176 cm^2 LNMO targets (Toshima manufacturing Co., Ltd.). The LNMO sputtered thin films were grown using different Ar-N_2 mixtures as process gas, namely LNMO_0% N_2, LNMO_50% N_2, LNMO_75% N_2, and LNMO_100% N_2, and following the deposition conditions listed in Table S1. The thickness of all LNMO thin films was 1 μm, which, as determined in a previous study, delivers the best electrochemical performance.[26] Following the growth conditions described in this previous study, the crystallization of the LNMO electroactive phase required post-annealing at 600 °C for one hour under air flow at a heating rate of 5 °C/min, using an alumina crucible as a sample container. After the thermal treatment, the samples were allowed to cool down freely.

Thin films physicochemical characterization

The atomic structure, phase, morphology and composition of the grown films have been characterized using a wide variety of experimental techniques. The atomic structure of the films was studied by means of X-ray diffraction (XRD) using a Bruker Advance D8 diffractometer with Co radiation (Co $K_{\alpha1,2}$ $\lambda = 1.78897$ Å, 1.79285 Å). The Rietveld refinement of the XRD patterns was performed using the FullProf software.[30] Raman spectroscopy was used to identify the obtained phase by means of a Renishaw InVia confocal microscope equipped with a 50x objective and a green (523 nm wavelength) laser with 2 μm spot size operating at 0.5 mW. The morphology was analyzed by Scanning Electron Microscopy (SEM) via a FEI Quanta-200FEG microscope at accelerating voltages between 10–30 kV. The surface roughness of the thin films was investigated by Atomic Force Microscopy (AFM), and the images were obtained using an Agilent 5500 microscope operated in tapping mode with Si tips (NT-MDT). AFM image analysis and calculation of the surface roughness were performed using Gwyddion software.[31] Further morphological and crystallographic characterization was performed on thin film powder scratched from the SS substrate using a FEI Tecnai G2 Transmission Electron Microscopy (TEM) instrument with a 200 kV field emission gun. Information about the elemental composition of the films was

ChemElectroChem

Research Article
doi.org/10.1002/celc.202201004

Chemistry Europe
European Chemical
Societies Publishing

obtained from Energy Dispersive X-ray spectroscopy (EDX) at the TEM microscope.

The samples' composition and local structure was probed by means of X-ray absorption spectroscopy (XAS) carried out at the 8.1 bending magnet (BEAR end-station BL8.1 L) of the ELETTRA synchrotron facility in Trieste (Italy). The spectral energy was calibrated using C $1s-\pi^*$ transitions. The incident light was unpolarized, and the incidence angle of the light with respect to the sample surface plane was kept fixed at 45°.[32] High-quality XAS measurements on the electrodes were performed in total electron yield mode.[33,34] The measurements were performed on various points of the sample to check for uniformity and possible degradation: no radiation damage was observed.

Cells assembling and electrochemical tests

Electrochemical characterization was conducted on CR2032 type coin cells (Hohsen Corp.) assembled inside an MBraun Ar filled globe box (H_2O and O_2 values below 0.1 ppm). The cells were composed of the grown LNMO thin films as working (positive) electrode and metallic lithium disks ($\emptyset = 14$ mm, Rockwood Lithium, battery grade, 99.8%) as counter and reference (negative) electrode. 1 M $LiPF_6$ in ethylene carbonate (EC)/dimethyl carbonate (DMC) (1:1 in volume) (Solvionic, 99.9%) was used as electrolyte and glass fiber (GE Healthcare, GF/D grade) as separator.

The long-term cycling performance of LNMO thin film electrodes was evaluated with a Maccor Series 4000 battery tester cycling the cells at a current rate of 1 C, where 1 C is assumed as 147 mAg^{-1} (with respect to active material mass). In the first six cycles, low current rates (C/10, C/5 and C/2, two cycles each) were used to ensure the proper formation of the electrode-electrolyte interphase (EEI). In addition, the response of the thin film electrodes at different current densities was also evaluated with a C-rate capability protocol that, after the formation cycles, started at C/10, increasing every five cycles up to 10 C (C/10, C/5, C/2, 1 C, 2 C, 5 C and 10 C), and straight back to C/10. Finally, the EEI stability, as well as the electronic and ionic transport properties, have been further studied by means of Electrochemical Impedance Spectroscopy (EIS), collecting impedance spectra of the cell during the initial charge every 25 mV in the frequency range of 15 mHz to 100 kHz. The measurements were performed using 3-electrode EL-CELL ECC-Ref cell applying 2 h of rest before EIS data acquisition to ensure equilibrium conditions.

Results and Discussion

Structural investigation

The spinel LNMO can crystallize in two different structures, namely ordered phase (S.G: $P4_332$) and disordered phase (S.G: $Fd3m$). The XRD patterns of the LNMO films grown by magnetron sputtering under different Ar-N_2 process atmospheres are presented in Figure 1. Due to the absence of some weak peaks at $2\theta \sim 24°$, 35°, 40°, 46°, 47°, and 57°, which are characteristic of the ordered structure,[18] the diffraction peaks can be indexed according to the structure of disordered spinel $LiMn_{1.5}Ni_{0.5}O_4$[35] Moreover, additional diffraction peaks were detected at 2θ around 43.5°, 44.5°, 50.7°, 64.7°, and 74.5° that correspond to stainless steel substrate (space group: $Fd3m$ and $Im-3m$). Besides this contribution, there are no distinguishable impurities.
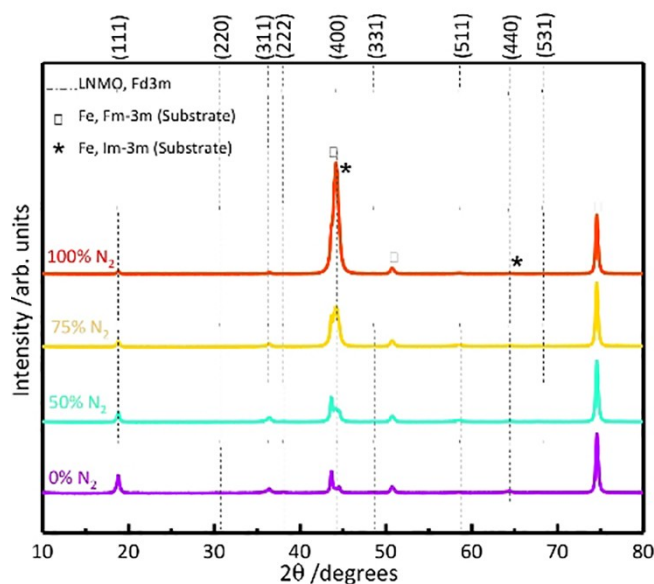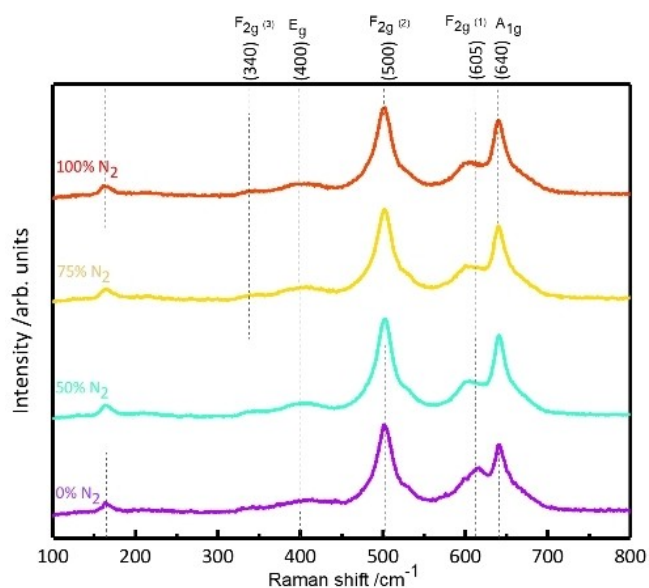

Figure 1. XRD patterns of LNMO thin films grown under different Ar-N_2 gas flow mixtures (0%, 50%, 75%, and 100%).

In fact, due to the similarities between both crystalline structures, the identification of the phase ordering by XRD is rather complex. In contrast, Raman spectroscopy is a suitable method to identify the phase ordering since it is highly sensitive to crystal symmetry.[35] The ordered spinel LNMO is expected to show the Raman vibrational modes A_{1g} (638 cm^{-1}), $F_{2g}^{(1)}$ (609 and 591 cm^{-1}), $F_{2g}^{(2)}$ (495 cm^{-1}), E_g (406 and 382 cm^{-1}), $F_{2g}^{(2)}$ (324 cm^{-1}) and two more modes at 241 and 221 cm^{-1}. Meanwhile the disordered spinel LNMO is expected to show the following vibrational modes: A_{1g} (636 cm^{-1}), $F_{2g}^{(1)}$ (597 cm^{-1}), $F_{2g}^{(2)}$ (496 cm^{-1}), E_g (399 cm^{-1}), and $F_{2g}^{(3)}$ (335 cm^{-1}).[36,37] The Raman spectroscopy results obtained from all the grown LNMO thin films are shown in Figure 2, where all the listed vibrational features can be observed. The vibrational modes A_{1g} (640 cm^{-1}), $F_{2g}^{(1)}$ (600 cm^{-1}), $F_{2g}^{(2)}$ (500 cm^{-1}), E_g (400 cm^{-1}), and $F_{2g}^{(3)}$ (340 cm^{-1}) appear in the Raman spectra, while the additional peaks at ~ 218 and 237 cm^{-1} corresponding to the ordered LNMO phase are not observed here,[38] suggesting that disordered spinel LNMO is obtained. The strong peak ~ 640 cm^{-1} is assigned to the stretching vibration mode of Mn–O, which corresponds to the vibrational stretching of the MnO_6 octahedral groups, while the peak around 600 cm^{-1} is attributed to the Ni–O band.[38,39] Meanwhile, the intensity of A_{1g} (640 cm^{-1}) is higher than the peak intensity of $F_{2g}^{(1)}$ (600 cm^{-1}) for all thin films, which confirms the existence of a disordered structure.[40] The strong peak around 500 cm^{-1} ($F_{2g}^{(2)}$) and the weak spectral feature at ~ 400 cm^{-1} (E_g) correspond to Ni^{2+}–O lattice bond vibrations.[38]

As confirmed by Raman and XRD results, all LNMO thin films display a disordered spinel structure. The XRD patterns were refined via the Rietveld method to determine the lattice parameter of the different LNMO thin films. The results are shown in Figure S2 of the Supplementary Information, XRD

Figure 2. Raman spectra of LNMO thin films grown under different Ar-N$_2$ gas flow mixtures (0%, 50%, 75%, and 100%).

patterns could be satisfactorily fitted using the *Fd3m* space group.

The lattice parameter of LNMO_50% N$_2$, LNMO_75% N$_2$, and LNMO_100% N$_2$ was found to be 8.201(2) Å, 8.1989(6) Å, and 8.171(1) Å respectively, which are slightly smaller than that of LNMO_0% N$_2$ (8.218(2) Å), suggesting that the lattice parameter decreases as the N$_2$ flow increases (Table 1).

These variations can be correlated with the entrapping of nitrogen into interstitial crystal sites,[41] compressing the structure and thus decreasing lattice parameters and cell volumes.

On the other hand, High Resolution TEM (HRTEM) was performed to investigate the LNMO structure via lattice spacing determination from Fast Fourier-Transform (FFT) of the HRTEM diffraction fringes. Thus, corroborating the disordered spinel structure for all thin films, shown in Figure 3. Indeed, for all samples LNMO_0%, 50%, and 100% N$_2$ (panels b, f, j in Figure 3), the lattice fringes can be correlated with the {111} interplanar spacing of the spinel phase. Electron diffraction rings were carefully analysed and indexed (panels c, d, g, h, k, l of Figure 3). The lattice rings of all samples indexed to (111), (220), (311), (222), (400), (133), (511), (044), (513), (444), (117), and (535) correspond to diffraction from LNMO spinel structure (Figure 3m). The diffraction rings of (111), (200), (202), (113),

and (222) planes are assigned to Fe-gamma from stainless steel substrate (Figure 3n), while the rings indexed as (110), (200), (112), and (220) correspond to Fe-alpha from stainless steel substrate (Figure 3o). The electron diffraction patterns are rather complex with many lattice rings very close to each other; however, it can be observed that the diameter of LNMO lattice rings slightly increased by increasing the N$_2$ concentration in the process gas, which further supports the LNMO lattice parameter decrease as nitrogen is introduced in the structure; in excellent agreement with the results obtained from Rietveld refinements of the XRD data.

In this study, EDX was used for the compositional analysis of LNMO. The results are shown in Figure S3 and Table S2 of the Supplementary Information. The results obtained from collecting the EDX spectra at two different positions (EDX1 and EDX2 in Figure S3) for every sample support the expected stoichiometry (LiNi$_{0.5}$Mn$_{1.5}$O$_4$). Low traces of light elements such as nitrogen are below the detection limit. This is why nitrogen can only be detected for the LNMO_100% N$_2$ sample.

To explore more in detail the thin films spinel structure and composition, XAS experiments were performed on LNMO_0% N$_2$, LNMO_50% N$_2$, and LNMO_100% N$_2$ samples. XAS measurements were carried out on the K edge of carbon, oxygen and nitrogen, and on the L edge of manganese and nickel.
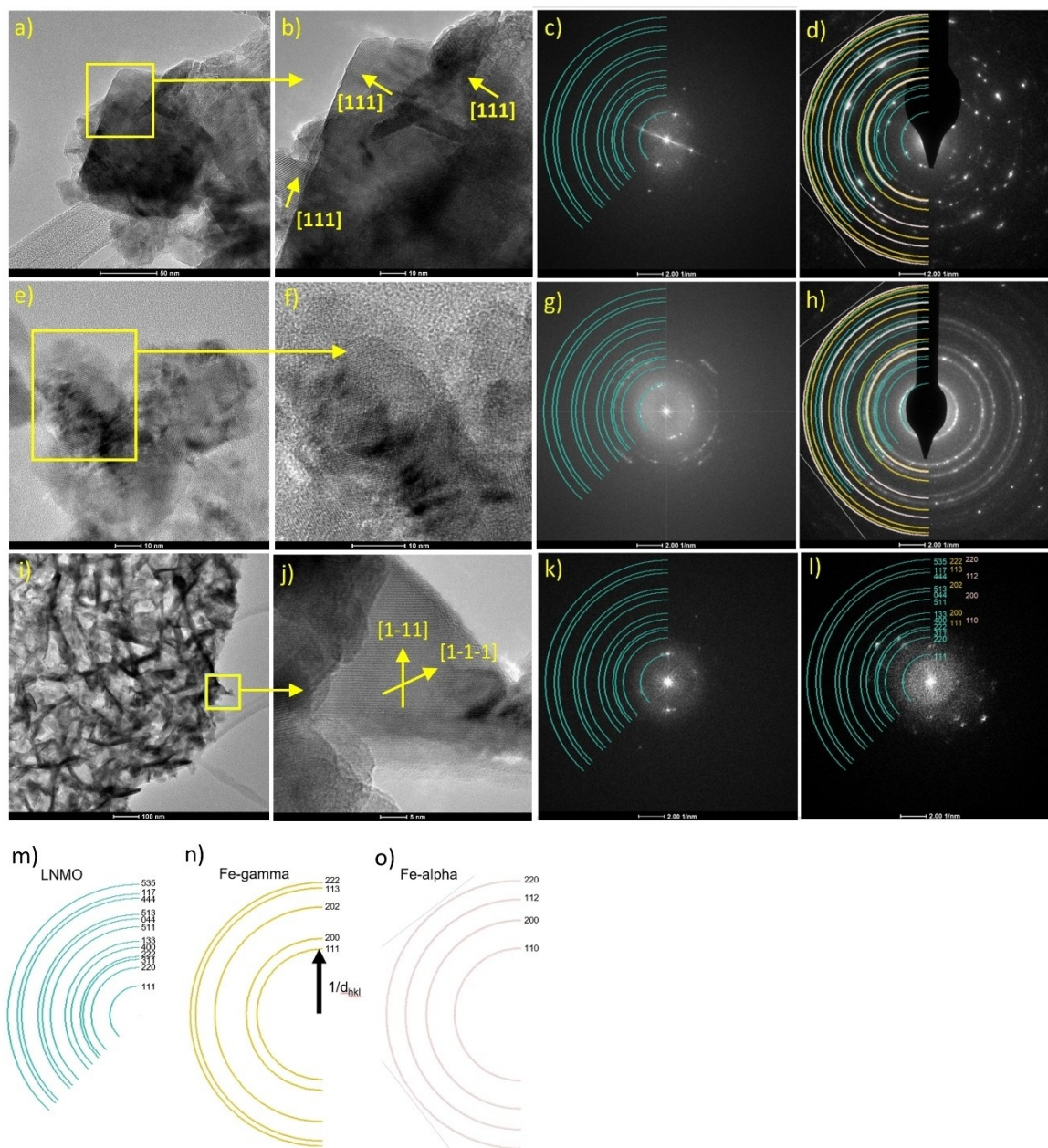
The XAS results indicate that the structure and chemistry of the LNMO remain stable upon nitridation. No significant change is observed in the C, O and Ni edges upon nitridation. Meanwhile, the Mn edge (Figure 4c) shows a minor broadening upon an increase of N flow in the process gas: being the peak width 2.20 eV for LNMO_0% N$_2$, 2.30 eV for LNMO_50% N$_2$ and 2.45 eV for LNMO_100% N$_2$. This broadening can be due to distortion of the crystalline structure and/or bond formation between Mn and N, increasing the Mn valence state. At the same time, the N edge (Figure 4e) reveals the presence of several peaks that could be assigned to C–N and O–N bonds from chemisorbed nitrogen.[42] However, we can assume that the eventual N chemisorption is the same for all samples. Therefore, since there is no evidence of N-based compounds, the increase of the component at ~401.5 eV upon increase of the nitrogen flow in the processing gas could be assigned to the insertion of the N into the structure interstitial sites. This would be in agreement with the XRD and TEM observations that report a decrease of the cell parameter upon nitrogen uptake.

Morphological investigation

Figure 5 depicts SEM images, recorded at two different magnifications (20000x and 40000x), of the LNMO thin films surface grown with different Ar/N$_2$ ratios in the process gas flow. As seen in the figure, except for the LNMO_100% N$_2$, all other LNMO thin films exhibit a homogeneous crystallite shape and size without cracks and pin holes. The crystallites have flake-like morphology, which may result in faster charge transfer kinetics of Li$^+$ ions.[9] With the addition of nitrogen to the process gas, the crystallites increase the surface area and the

Table 1. Unit cell parameter and cell volume of LNMO thin films grown under different Ar-N$_2$ gas flow mixtures (0%, 50%, 75%, and 100%).		
Sample	Lattice parameter [Å]	Cell volume [Å^3]
0% N$_2$	8.218(2)	555.081
50% N$_2$	8.201(2)	551.582
75% N$_2$	8.1989(6)	551.143
100% N$_2$	8.171(1)	545.567

ChemElectroChem

Research Article
doi.org/10.1002/celc.202201004
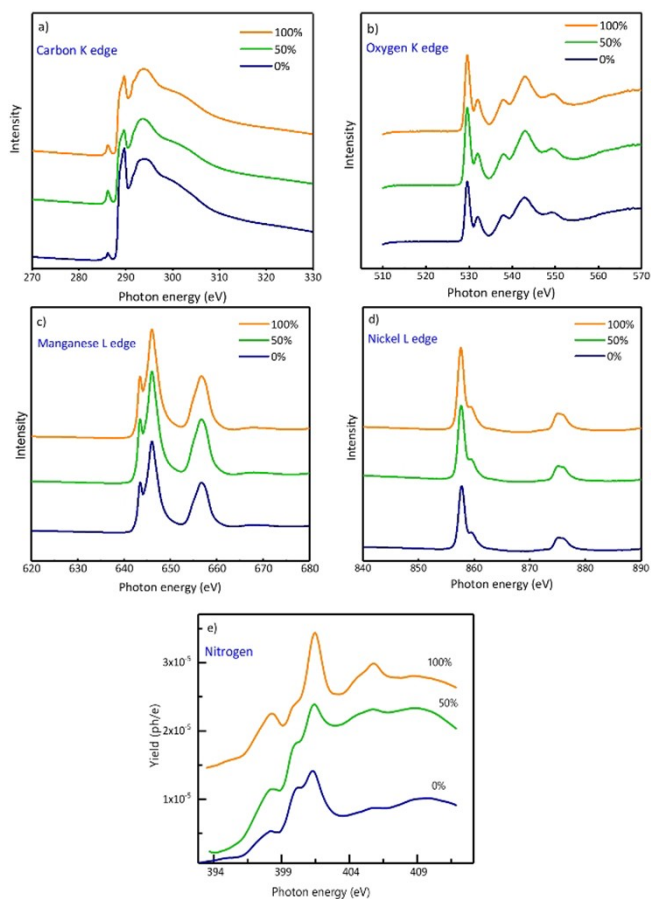
Chemistry
Europe

European Chemical
Societies Publishing

Figure 3. TEM images of LNMO thin films with different Ar/N$_2$ ratio in the process gas flow, corresponding to LNMO_0% N$_2$ (a–d), LNMO_50% N$_2$ (e–h), LNMO_100% N$_2$ (i–l), and indexation of the diffraction rings for the identified phases (m–o).

flake-like morphology is more pronounced (Figure 5c,d). Further addition of nitrogen into the process gas resulted in more changes in the surface morphology where the crystallites reduced their size while keeping the flake-like morphology, as presented in Figure 5e–h. This morphology change can be due to the combination of two effects, on the one side, the presence of nitrogen in the sputtering atmosphere can decrease the kinetic energy and mobility of the transition metal adatoms, because of the affinity of nitrogen with transition metals,[43] on the other side, by decreasing the Ar concentration in the process gas, the diffusion rate of N$_2$ along the grain boundary sites decreases,[44] as a result, the arrangement into larger crystals may be hindered, and more discontinuities in the

crystallite morphology are introduced, resulting into smaller powder gains. This behavior is confirmed by XRD patterns, where significant intensity loss and broadening of the diffraction peaks can observed when increasing the N$_2$ flux.

Despite the morphology changes, all the thin films show uniform morphology across the sample, which might be an essential benefit in terms of electrochemical performance because the LNMO can be capable of buffering the volume change of Jahn-Teller distortions associated with the spinel structure.[9]
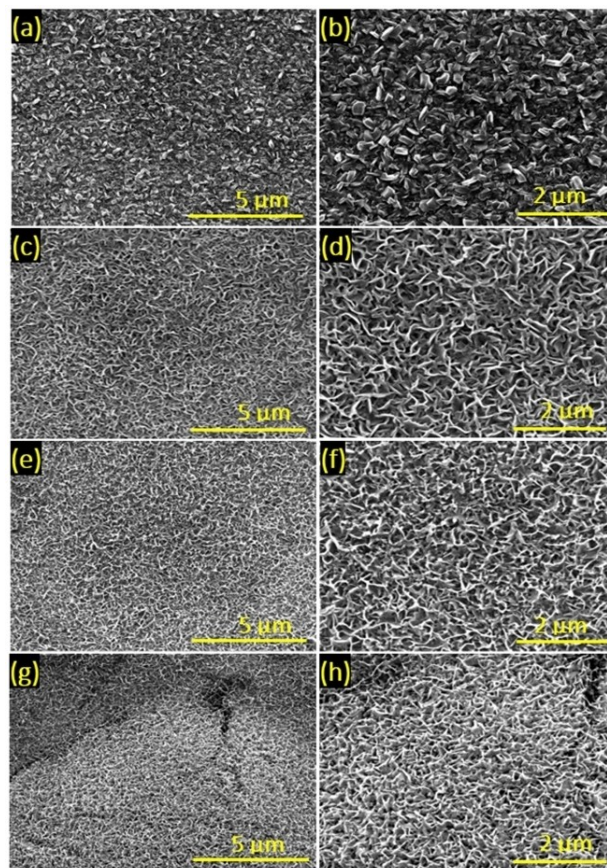
Since some cracks were observed at high magnification (Figure 5g), additional SEM images were recorded at lower magnifications of 1000x and 2000x, as shown in Figure S4, to

ChemElectroChem

Research Article
doi.org/10.1002/celc.202201004

Chemistry Europe
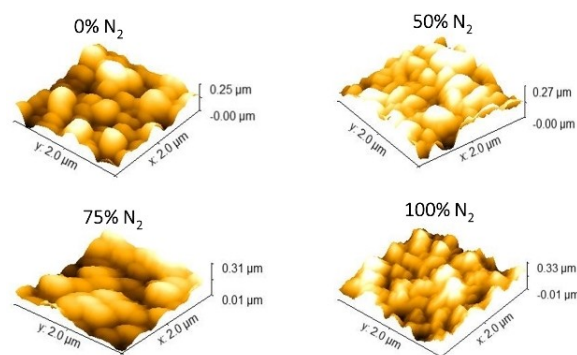European Chemical
Societies Publishing

Figure 4. XAS spectra collected on the carbon K edge (a), oxygen K edge (b), manganese L edge (c), nickel L edge (d) and nitrogen K edge (e) for LNMO_0% N_2 (blue), LNMO_50% N_2 (green), and LNMO_100% N_2 (orange) thin films.

Figure 5. SEM images of the surface of the LNMO thin films grown with different ratio of Ar-N_2 flow, corresponding to LNMO_0% N_2 (a,b), LNMO_50% N_2 (c,d), LNMO_75% N_2 (e,f), and LNMO_100% N_2 (g,h). Images have been recorded at two magnifications: 20000x and 40000x.

obtain more information on the surface of the thin films when using N_2 flows above 75%: samples LNMO_75% N_2 and LNMO_100% N_2. At these low magnifications, bubbles can be seen on the surface of both samples. This would be in agreement with the presence of gaseous species, which expanded from the subsurface region towards the surface of the films during heat treatment, resulting in the observed surface irregularities. The sample grown with 100% N_2 (Figure S4c,d) appears to have larger bubbles on the surface than the sample grown with 75% N_2 (Figure S4a,b). The presence of bubbles suggests that, when growing the film with high N_2 flux, part of the nitrogen cannot be incorporated into the lattice structure of LNMO. Moreover, the bubbles would hinder the interparticle contact of the LNMO crystallites.

Following morphological investigations, to provide further insights into the surface morphology evolution and roughness of the LNMO thin films, tapping-mode AFM measurements were carried out. In order to ensure that the AFM results represent the whole sample, several points over the sample were probed. The 3D surface morphology of the thin films is illustrated in Figure 6, where the surface features of the different thin films can be observed.


Figure 6. 3D surface morphology of the LNMO thin films grown with different Ar-N_2 flow ratio.

Furthermore, the AFM amplitude images of the thin films (Figure S5a), which provide better insight into morphological features and edges, and AFM topography (Figure S5b), used to measure the average roughness of the surface (the obtained values are listed in Table S3) are all included in the Supporting Information. AFM observations have shown that the thin film crystallite size decreases when adding 50% N_2 flow, representing a 2D crystal growth, which is in good agreement with the

ChemElectroChem

Research Article
doi.org/10.1002/celc.202201004

**Chemistry
Europe**
European Chemical
Societies Publishing

results obtained by SEM. The increase of surface roughness (Table S3) is detected for the film processed only with 100% N_2 flow (100% N_2), which can be due to the surface defects (formation of cracks) already observed by SEM. These surface defects might be related to the fact that in the LNMO_100% N_2, there is an excess of N_2 flux, where this excess is releasing from the materials creating cracks. As a result, the AFM results confirm the SEM observations and complement the information.

Electrochemical investigation

To evaluate the effect of nitridation on the electrochemical performance and cycling stability, all LNMO thin films were galvanostatically tested at 1 C rate in the operating voltage window 3.5–4.85 V *vs.* Li$^+$/Li (low current rates – C/10, C/5 and C/2, two cycles each - were used in the first six cycles for electrode conditioning), shown in Figure 7a. Regarding the delivered initial discharge capacity upon electrochemical cycling at 1 C after activation, the LNMO_0% N_2, LNMO_50% N_2,
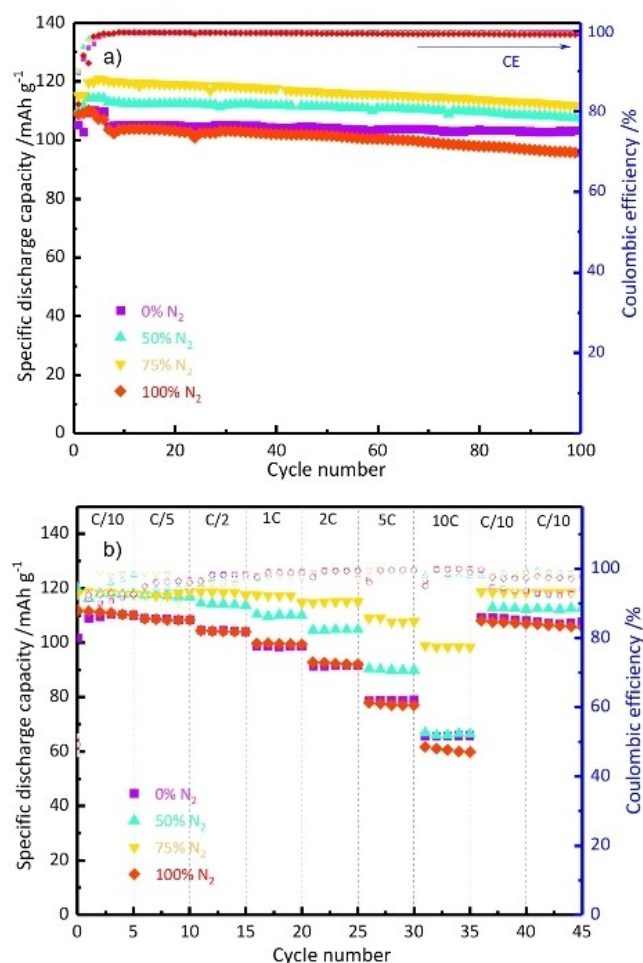
Figure 7. Electrochemical performance of thin films made in mixture Ar-N_2 flow containing N_2 flow at a ratio of 0%, 50%, 75%, and 100% : cycling performance (a), and rate capability (b) in the operating voltage range of 3.5–4.85 V *vs.* Li$^+$/Li.
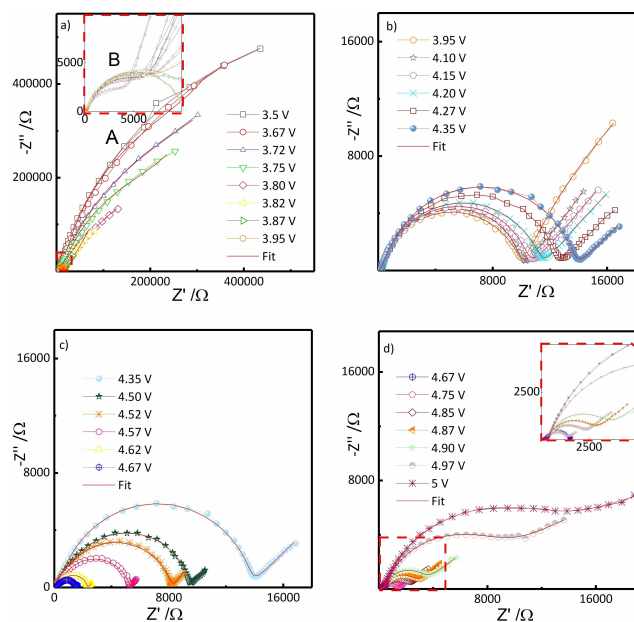
LNMO_75% N_2, and LNMO_100% N_2 exhibit an initial discharge capacity of 104.7, 112.9, 120.0, and 104.5 mAh g^{-1}, respectively.

To evaluate the response of the thin films at different current densities, the LNMO thin films were tested to find their C-rate capability, charged and discharged from C/10 to 10 C and back to C/10 in the 3.5 - 4.85 V *vs.* Li$^+$/Li voltage window. Figure 7b presents the discharge capacity as a function of the current density rate. According to these results, the LNMO_75% N_2 electrode delivers the best rate performance at all C-rates.

The LNMO-75% N_2 electrode shows a high discharge capacity of 120 mAh g^{-1} at C/10 and 99 mAh g^{-1} at 10 C. In contrast, 104 mAh g^{-1} at C/10 and 65.6 mAh g^{-1} at 10 C is delivered by LNMO_0% N_2. The coulombic efficiencies of LNMO_75% N_2 at C/10 (at initial cycle) and 10 C are 51.87% and 98.78%, respectively, while LNMO_0% N_2 exhibits lower coulombic efficiency values of 47.2% and 96.5% at the same C-rates. The superior rate performance of LNMO_75% N_2 could be attributed, on the one hand, to the enhanced conductivity of cells resulting from N insertion and, on the other hand, to the observed morphological and structural properties, where the smaller particle size improves the Li$^+$-ion diffusion. The electrodes grown with 0% and 100% N_2 flow have similar C-rate capability profiles, while LNMO_50% N_2 delivers higher capacity and better rate performance at different current densities.

The long-term stability of the LNMO_0% N_2 and LNMO_50% N_2 were evaluated at a higher cut-off voltage of 5 V by cycling the cells at 1 C for 700 cycles, and the results are shown in Figure S6 of the Supplementary Information. Again, the first 6 cycles were electrode conditioning cycles at low current densities. The LNMO_0% N_2 and LNMO_50% N_2 at 1 C in the voltage range between 3.5 V and 5 V deliver, after the activation cycles, initial discharge capacity values of 114 and 120 mAh g^{-1}, respectively. After 700 cycles, LNMO_0% N_2 and LNMO_50% N_2 exhibit reversible discharge capacity of 84.3 and 86.2 mAh g^{-1}, corresponding to a capacity retention of 74% and 72%, respectively. In the 1st and 700th cycle, the corresponding coulombic efficiencies of both thin films are similar, with values around 50% and 98%, respectively. It should be mentioned that LNMO_75% N_2 exhibits a considerable drop in the specific discharge capacity when cycled at cut-off voltage of 5 V. This can be due to the accumulation of side products generated from electrolyte decomposition, as expected in materials with small particle size (high surface area), which ultimately results in poor cycling performance.

In order to shed light on the Li$^+$-ion kinetics upon electrochemical cycling, electrochemical impedance spectroscopy (EIS) characterization has been carried out by collecting sequences of EIS spectra during the first oxidation for LNMO_0% N_2 and also for N-containing LNMO_50% N_2 owing to its good performance at both cut-off voltages, namely 4.85 and 5 V vs. Li$^+$/Li. The selected sequences of Nyquist plots corresponding to the relevant potentials for the LNMO_0% N_2 are shown in Figure 8, while Nyquist plots for the LNMO_50% N_2 are illustrated in Figure 9. The Nyquist plots present the typical features of cathode electrodes for LIBs.[45–48] It can be observed at a glance that the LNMO_50% N_2 shows one order of magnitude lower overall resistance values compared to that of

ChemElectroChem

Research Article
doi.org/10.1002/celc.202201004

Chemistry
Europe
European Chemical
Societies Publishing

Figure 8. The corresponding Nyquist plots for LNMO_0% N$_2$ during the first oxidation at different voltage values.
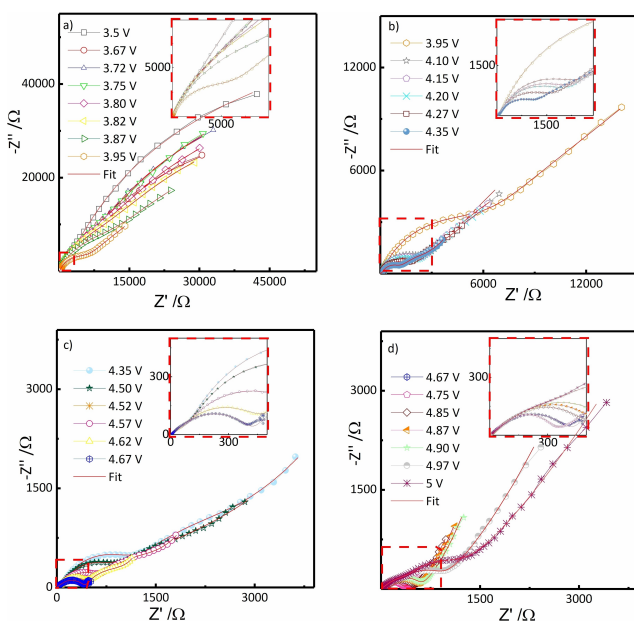
Figure 9. The corresponding Nyquist plots for LNMO_50% N$_2$ during the first oxidation at different voltage values.
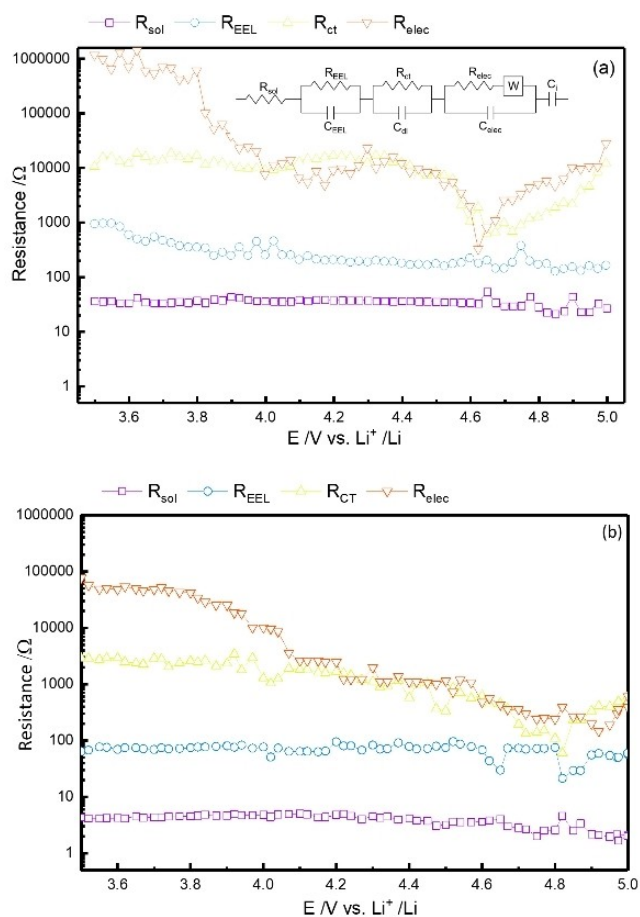
the LNMO_0% N$_2$. However, both cells show a similar trend during operation. The Nyquist plots in Figs. 8a and 9a reveal that at 3.5 V ≤ E ≤ 3.95 V, a large arc is developed at low-frequency (labelled as A in Figure 8a), and two overlapped semicircles at middle- and high- frequencies (denoted as B in the inset). Panels 'A' reveal that by increasing the potential, in other words extracting the Li$^+$-ions, the low-frequency arc starts to bend towards the real axis. However, as the deintercalation proceeds and the potential is further increased in the range from 3.95 V to 4.35 V vs. Li$^+$/Li (Figure 8b), the overall

impedance starts increasing for the LNMO_0% N$_2$. This can be due to the transition between multiple cubic phases of LNMO.[49] In the 4.35–4.67 V vs. Li$^+$/Li voltage range, Figure 8c demonstrates that the overall impedance drops for the LNMO_0% N$_2$ sample. In the case of LNMO_50% N$_2$, shown in Figure 9a–c, as the potential approaches to the beginning of the deintercalation peak (3–4.67 V vs. Li$^+$/Li), the overall impedance spectra and the large arc at low-frequency progressively become smaller. The decrease of the low-frequency semicircle resistance values can be correlated with the phase transitions that occur on the LNMO upon Li$^+$-ion extraction. Above 4.67 V vs. Li$^+$/Li (Figures 8d, 9d), the trend to form a great arc "A" in the low-frequency region can be observed for both samples, which can be due to the formation of the rock salt-like LNMO phase: for the LNMO_0% N$_2$ sample, this behaviour is more evident.[49]

In order to clarify this behaviour and distinguish the contribution of each process to the overall resistance values, all the impedance spectra have been fitted to the equivalent circuit of $R_{sol}(R_{EEL}C_{EEL})(R_{CT}C_{DL})([R_{elec}W]C_{elec})C_i$ in Boukamp's notation[50] with RelaxIS software (rhd instruments, Germany). The R_{sol} represents the electrolyte resistance at the highest frequency intercept. R_{EEL} and C_{EEL} are related to the resistance and capacitance of the electrode-electrolyte interphase (a semicircle at high-frequencies), R_{CT} and C_{DL} to the charge-transfer process, and double layer capacitance (a semicircle at middle frequencies), and R_{elec} corresponds to the electronic resistance with the associated capacity (C_{elec}) from the charge accumulation at the surface of the particles and/or at intra-particle crystallite domains (the third semicircle at low-frequency, marked as A). The W (Warburg diffusion) and C_i (intercalation capacity) are observed by sloped line at the lowest frequencies associated to Li$^+$-ion diffusion to a blocking electrode. To consider any inhomogeneities or roughness of the electrodes, all the C elements have been replaced by constant-phase elements Q.

The trend of each resistance value determined by the EIS fitting is shown in Figure 10a,b for LNMO_0% N$_2$ and LNMO_50% N$_2$, respectively. As previously observed in Nyquist plots, all resistance values, i.e., R_{sol}, R_{EEL}, R_{CT}, and R_{elec}, decreased with nitrogen doping. The R_{elec} drops for both cells upon Li$^+$-ion extraction. However, the R_{elec} values of LNMO_0% N$_2$ (Figure 10a) show some oscillations in the range of 3.95–4.35 V vs. Li$^+$/Li. This suggests a lattice rearrangement (the evolution of multiple cubic phases), leading to poor Li$^+$-ion diffusion in the LNMO spinel, consistently with the results from Li et al.[49] Besides, at a higher 4.67 V vs. Li$^+$/Li, the R_{elec} increased. This may be related to the well-known formation of a rock salt-like phase at high voltages due to the migration of some transition metal ions from 16d to 16c sites.[49] Even so, comparing the R_{elec} at the lithiated state to that of the delithiated state, the lower values obtained at 5.0 V suggested that the LNMO becomes less electronically insulator by extracting Li$^+$-ion. This is related to the fact that the conducting domains become rapidly interconnected.[45,47,51,52] The mentioned phase transitions of LNMO_0% N$_2$ seem to be suppressed by nitrogen doping, as suggested the R_{elec}, (Figure 10b). This is due to the fact that the

ChemElectroChem

Research Article
doi.org/10.1002/celc.202201004

Chemistry Europe
European Chemical
Societies Publishing

Figure 10. The fitted resistance values during the first charge, a) LNMO_0% N$_2$ and b) LNMO_50% N$_2$.

diffusion of Li$^+$-ion enhances the stability of the charge transfer interfaces via decreasing lattice mismatch and structural stress upon the charge and discharge.[49]

In the case of R_{CT} values, both samples show relatively constant values. However, as in the case of R_{elec} values of LNMO_0% N$_2$, R_{CT} values increase in the 3.95–4.35 V vs. Li$^+$/Li. The increase can be due to the fact that R_{CT} also affects by the phase transitions and changes due to rearrangements of the electrode-electrolyte interface. Moreover, when further Li$^+$-ions are extracted (4.67 V vs. Li$^+$/Li), the R_{CT} values increase again. This can be due to rock salt-like phase formation. Meanwhile, the LNMO_50% N$_2$ thin film exhibits lower and more constant R_{CT} values upon the 1st delithiation, where it decreases up to 4.85 V and then slightly increases up to 5 V due to structural rearrangement.

Finally, the R_{EEI} and R_{sol} are constant upon the 1st oxidation for both samples. However, the R_{EEI} and R_{sol} values for the LNMO_50% N$_2$ thin film are around one order of magnitude lower than the LNMO_0% N$_2$ thin film, in agreement with the higher Coulombic efficiency values. These results suggest a more stable electrode /electrolyte interfacial behaviour.

Conclusions

The MF-AC magnetron sputtering facile synthetic method, a prominent candidate for thin-film battery industrial production, was proposed for the preparation of LiNi$_{0.5}$Mn$_{1.5}$O$_4$ (LNMO) cathode materials with highly morphology-controllable size, and crystal particle growth. The nitridation process was proposed to improve the electrical conductivity and electrochemical behaviour by preparing thin films in Ar-N$_2$ mixtures, namely LNMO_0% N$_2$, LNMO_50% N$_2$, LNMO_75% N$_2$, and LNMO_100% N$_2$.The Raman spectra and XRD studies confirmed the disordered structure of all LNMO thin films. According to SEM and TEM images, the particle size decreased by adding nitrogen into the process gas. The partial nitrogen could not be incorporated into the lattice structure of LNMO_100% N$_2$, resulting in cracks on the film's surface during annealing and a high roughness value. The specific discharge capacity values and rate capability were enhanced by further increasing the Ar/N$_2$ ratio to 50% and 75% due to their enhanced morphological and structural characteristics, and improved conductivity. According to EIS results, nitridation had considerable impact on enhancing electronic and electrochemical performances and on suppressing the phase transitions. These results would support the integration of N in the LNMO structure, so the electrochemical performance of this cathode material was improved, particularly its interfacial stabilization.

Indeed, this is a route that must be optimized if high voltage positive electrodes are to be used in Li-ion batteries with higher energy density and much less dependence on critical raw materials such as Co.

Conflict of Interest

The authors declare no conflict of interest.

Data Availability Statement

The data that support the findings of this study are available on request from the corresponding author. The data are not publicly available due to privacy or ethical restrictions.

ChemElectroChem

Research Article
doi.org/10.1002/celc.202201004

Chemistry Europe
European Chemical
Societies Publishing

[1] N. Nitta, F. Wu, J. T. Lee, G. Yushin, *Mater. Today* **2015**, *18*, 252.

[2] Y. Chen, Y. Tian, Y. Qiu, Z. Liu, H. He, B. Li, H. Cao, *Mater. Today* **2019**, *1*, 100001.

[3] A. M. Hashem, S. M. Abbas, X. Hou, A. E. Eid, A. E. Abdel-Ghany, *Heliyon* **2019**, *5*, e02027.

[4] P. Chand, V. Bansal, Sukriti, V. Singh, *J. Sci. Adv. Mater. Devices* **2019**, *4*, 245.

[5] H. Berg, K. Göransson, B. Noläng, J. O. Thomas, *J. Mater. Chem.* **2000**, *10*, 1437.

[6] L. Chen, R. E. Warburton, K. S. Chen, J. A. Libera, C. Johnson, Z. Yang, M. C. Hersam, J. P. Greeley, J. W. Elam, *Chem* **2018**, *4*, 2418.

[7] S. Wang, C. Luo, Y. Feng, G. Fan, L. Feng, M. Ren, B. Liu, *Ceram. Int.* **2020**, *46*, 13003.

[8] Y. Yu, M. Xiang, J. Guo, C. Su, X. Liu, H. Bai, W. Bai, K. Duan, *J. Colloid Interface Sci.* **2019**, *555*, 64.

[9] J. Lu, K. S. Lee, *Mater. Technol.* **2016**, *31*, 628.

[10] X. Zheng, W. Liu, Q. Qu, H. Zheng, Y. Huang, *J. Mater.* **2019**, *5*, 156.

[11] Y. He, J. Zhang, Q. Li, Y. Hao, J. Yang, L. Zhang, C. Wang, *J. Alloys Compd.* **2017**, *715*, 304.

[12] M. Y. Abeywardana, N. Laszczynski, M. Kuenzel, D. Bresser, S. Passerini, B. Lucht, *Int. J. Electrochem.* **2019**, *2019*, 8636540.

[13] S. Bhuvaneswari, U. V. Varadaraju, R. Gopalan, R. Prakash, *Electrochim. Acta* **2019**, *327*, 135008.

[14] G. Ganas, G. Kastrinaki, D. Zarvalis, G. Karagiannakis, A. G. Konstando-poulos, D. Versaci, S. Bodoardo, *Mater. Today: Proc.* **2018**, *5*, 27416.

[15] K. Raju, F. P. Nkosi, E. Viswanathan, M. K. Mathe, K. Damodaran, K. I. Ozoemena, *Phys. Chem. Chem. Phys.* **2016**, *18*, 13074.

[16] J. Yoon, M. Jeong, I. T. Bae, K. W. Nam, W. S. Yoon, *J. Power Sources* **2017**, *368*, 1–10.

[17] S. Liu, Z. Dang, D. Liu, C. Zhang, T. Huang, A. Yu, *J. Power Sources* **2018**, *396*, 288.

[18] T. F. Yi, J. Mei, Y. R. Zhu, *J. Power Sources* **2016**, *316*, 85.

[19] S. H. Ju, Y. C. Kang, Y. K. Sun, D. W. Kim, *Mater. Chem. Phys.* **2012**, *132*, 223.

[20] Z. Chen, S. Qiu, S. Cao, X. Ai, K. Xie, X. Hong, H. Yang, *J. Mater. Chem.* **2012**, *22*, 17768.

[21] H. Zhou, X. Ding, G. Liu, Z. Gao, G. Xu, X. Wang, *RSC Adv.* **2015**, *5*, 108007.

[22] N. Arun, V. Aravindan, S. Jayaraman, N. Shubha, W. C. Ling, S. Ramakrishna, S. Madhavi, *Nanoscale* **2014**, *6*, 8926.

[23] G. Wang, J. Xie, T. Zhu, G. Cao, X. Zhao, S. Zhang, *Funct. Mater. Lett.* **2014**, *7*, 1450009.

[24] X. Zhang, F. Cheng, J. Yang, J. Chen, *Nano Lett.* **2013**, *13*, 2822.

[25] Y. Liu, J. Li, M. Zeng, Y. Huang, X. Xu, M. Yan, J. Guo, J. Deng, J. Yang, *Ceram. Int.* **2018**, *44*, 20043.

[26] J. Rikarte, I. Madinabeitia, G. Baraldi, F. J. Fernández-Carretero, V. Bellido-González, A. García-Luis, M. Á. Muñoz-Márquez, *Adv. Mater. Interfaces* **2021**, *2002125*, 1–10.

[27] H. Z. Zhang, Q. Q. Qiao, G. R. Li, S. H. Ye, X. P. Gao, *J. Mater. Chem.* **2012**, *22*, 13104.

[28] S. Yoon, *J. Appl. Electrochem.* **2016**, *46*, 479.

[29] J. B. Bates, N. J. Dudney, G. R. Gruzalski, R. A. Zuhr, A. Choudhury, C. F. Luck, J. D. Robertson, *Solid State Ionics* **1992**, *647*, 53–56.

[30] J. Rodríguez-Carvajal, *Phys. B: Condens. Matter* **1993**, *192*, 55.

[31] D. Nečas, P. Klapetek, *Cent. Eur. J. Phys.* **2012**, *10*, 181.

[32] S. J. Rezvani, A. D'Elia, S. Macis, S. Nannarone, S. Lupi, F. Schütt, F. Rasch, R. Adelung, B. Lu, Z. Zhang, L. Qu, X. Feng, A. R. Vázquez, A. Marcelli, *Diamond Relat. Mater.* **2021**, *111*, 108171.

[33] S. J. Rezvani, F. Nobili, R. Gunnella, M. Ali, R. Tossici, S. Passerini, A. Di Cicco, *J. Phys. Chem. C* **2017**, *121*, 26379.

[34] S. J. Rezvani, R. Parmar, F. Maroni, F. Nobili, A. Di Cicco, R. Gunnella, *J. Phys. Chem. C* **2020**, *124*, 26670.

[35] Y. F. Deng, S. X. Zhao, Y. H. Xu, K. Gao, C. W. Nan, *Chem. Mater.* **2015**, *27*, 7734.

[36] L. Wang, H. Li, X. Huang, E. Baudrin, *Solid State Ionics* **2011**, *193*, 32.

[37] Y. H. Xu, S. X. Zhao, Y. F. Deng, H. Deng, C. W. Nan, *J. Mater.* **2016**, *2*, 265.

[38] N. Amdouni, K. Zaghib, F. Gendron, A. Mauger, C. M. Julien, *Ionics* **2006**, *12*, 117.

[39] D. Liu, W. Zhu, J. Trottier, C. Gagnon, F. Barray, A. Guerfi, A. Mauger, H. Groult, C. M. Julien, J. B. Goodenough, K. Zaghib, *RSC Adv.* **2014**, *4*, 154.

[40] A. Wei, W. Li, Q. Chang, X. Bai, R. He, L. Zhang, Z. Liu, Y. Wang, *Electrochim. Acta* **2019**, *323*, 134692.

[41] E. Salahinejad, R. Amini, M. Ghaffari, M. J. Hadianfard, *J. Alloys Compd.* **2010**, *505*, 584.

[42] Y. Shang, K. Feng, Y. Wang, X. Sun, J. Zhong, *RSC Adv.* **2019**, *9*, 11552.

[43] S. R. Kappaganthu, Y. Sun, *Appl. Phys. A Mater. Sci. Process.* **2005**, *81*, 737.

[44] K. Abbas, R. Ahmad, I. A. Khan, S. Saleem, U. Ikhlaq, *Int. J. Mater. Metall. Eng.* **2016**, *10*, 858.

[45] H. Darjazi, S. J. Rezvani, S. Brutti, F. Nobili, *Electrochim. Acta* **2021**, *139577*.

[46] F. Nobili, R. Tossici, F. Croce, B. Scrosati, R. Marassi, *J. Power Sources* **2001**, *94*, 238.

[47] F. Nobili, S. Dsoke, F. Croce, R. Marassi, *Electrochim. Acta* **2005**, *50*, 2307.

[48] F. Nobili, S. Dsoke, M. Minicucci, F. Croce, R. Marassi, *J. Phys. Chem. B* **2006**, *110*, 11310.

[49] J. Li, H. Wang, W. Dong, Z. Shi, W. Xie, H. Qiao, Q. Yu, M. Zhang, J. Hu, L. Yang, J. Hong, *J. Phys. Chem. C* **2018**, *122*, 25229.

[50] B. A. Boukamp, *Solid State Ionics* **1986**, *20*, 31.

[51] H. Darjazi, E. Gonzalo, B. Acebedo, R. Cid, M. Zarrabeitia, F. Bonilla, M. Á. Muñoz-Márquez, F. Nobili, *Mater. Today Sustain.* **2022**, *20*, 100236.

[52] F. Nobili, F. Croce, R. Tossici, I. Meschini, P. Reale, R. Marassi, *J. Power Sources* **2012**, *197*, 276.